

Discovery of Gamma-Ray Emission from the X-shaped Bulge of the Milky Way

Oscar Macias*,¹ Chris Gordon,² Roland M. Crocker,³ Brendan Coleman,²
Dylan Paterson,² Shunsaku Horiuchi,¹ & Martin Pohl^{4,5}

¹Center for Neutrino Physics, Department of Physics, Virginia Tech, Blacksburg, VA 24061, USA,

²Department of Physics and Astronomy, Rutherford Building,
University of Canterbury, Private Bag 4800, Christchurch 8140, New Zealand,

³Research School of Astronomy and Astrophysics,
Australian National University, Canberra, Australia,

⁴Institute of Physics and Astronomy, University of Potsdam, 14476 Potsdam-Golm, Germany,

⁵DESY, Platanenallee 6, 15738 Zeuthen, Germany

An anomalous signal has been found in Fermi Gamma-Ray Large Area Telescope data covering the center of the Galaxy. Given its morphological and spectral characteristics, this ‘Galactic Center Excess’ is ascribable to self-annihilation of dark matter particles. We report on an analysis that exploits hydrodynamical modeling to register the position of interstellar gas associated with diffuse Galactic γ -ray emission. Our improved analysis reveals that the excess γ -rays are spatially correlated with both the X-shaped stellar over-density in the Galactic bulge and the nuclear stellar bulge. Given these correlations, we argue that the Galactic Center gamma-ray excess is not a dark matter phenomenon but rather associated with the stellar population of the bulge and the nuclear bulge.

An extended γ -ray signal, not readily attributable to known Galactic sources, has been found [1, 2, 3, 4, 5, 6, 7, 8, 9] in Fermi Gamma-Ray Large Area Telescope (Fermi-LAT) data covering the central $\sim 10^\circ$ of the Galaxy. This Galactic Center Excess (GCE) signal has a spectral peak at ~ 2 GeV and reaches its maximum intensity at the Galactic Center (GC) from where it falls off as a radial power law $\propto r^{-2.4}$. Given its morphological and spectral characteristics, the GCE emission is consistent with self-annihilation of dark matter particles governed by a Navarro-Frenk-White (NFW) like density profile. However, it could also be composed of many dim, unresolved point sources for which millisecond pulsars (MSPs) [3, 5, 10] or pulsars [11] would be natural candidates

*To whom correspondence should be addressed. E-mail: oscar.macias@vt.edu

given their GeV-peaked gamma-ray spectra. Previous studies have also claimed significant non-sphericity for the GCE [12] or extended emission spectrally similar to the GCE from the Galactic plane [13, 14]; both of these suggest the GCE has an astrophysical origin.

The main challenge in pinning down the properties of GC γ -ray emission is correct modeling of diffuse Galactic emission from the interaction of cosmic rays with interstellar gas and radiation fields, by far the dominant source of γ -rays in this sky region. The Fermi-LAT Collaboration designed a diffuse Galactic emission model based on a model-fitting template approach that is optimized to single out γ -ray point sources in the data [15]. This presupposes that the diffuse Galactic emission can be modeled as a linear combination of interstellar gas, inverse Compton (IC) maps, and several other diffuse components. Due to the limited kinematic resolution of gas tracers towards the GC, interstellar gas correlated photons from this direction are particularly difficult to disentangle. Previous works utilized interstellar gas maps that were constructed with an interpolation approach that assumes circular motion of interstellar gas in the inner few degrees of the GC. This kinematic assumption provides for an estimate of the distance to a given gas cloud. However, it is well established that the Galaxy contains a central bar which causes non-circular motion of interstellar gas in the inner Galaxy, so assuming circularity introduces a significant and avoidable bias to γ -ray analyses of the region [16].

Here, we present a novel analysis of Fermi-LAT data accumulated between August 4, 2008 and September 4, 2015 in the $15^\circ \times 15^\circ$ region around the GC. Details of event selections as well as the fitting method used in this analysis are discussed at length in the Appendix. We used state-of-the-art hydrodynamical simulations [16] that account for the dynamical effects of the Galactic bar so as to better determine the contributions of diffuse and discrete sources of high-energy γ -rays. Gas maps informing our diffuse emission modeling were constructed by specifying a probabilistic deconvolution method for assigning gas clouds to distances via hydrodynamic gas flow model predictions. To critically evaluate the impact that the choice of interstellar gas models have on our results we constructed atomic and molecular hydrogen gas maps using an interpolation approach that reproduced those used in most previous γ -ray analyses of the GC [17]. Full details on the diffuse Galactic emission model components we used are provided in the Appendix.

Our analysis was performed using the Fermi-LAT Science Tools [22]. We used a bin-by-bin analysis technique [18] in which we split the LAT data into 19 energy windows to determine the significance of a source and to fit spectral parameters. Recent studies [23, 24] pointed out that additional, unresolved, point-like sources seen as dim clusters of photons could have a large influence on the fitted spectrum and spatial morphology of the GCE. In order to search for such objects we divided the region of interest in $0.1^\circ \times 0.1^\circ$ grid positions and examined the significance of a trial point source. The outcome of this pass was a residual test statistic (TS) map. The TS at each pixel was computed as $TS = 2(\log \mathcal{L}(\text{source}) - \log \mathcal{L}(\text{no-source}))$, where \mathcal{L} is the maximum likelihood of the data given the model with or without a source present at a given grid position. The detection significance is given by the square-root of the equivalent TS for one new degree of freedom [25]. In accordance with our bin-by-bin method, a residual TS map was computed for each energy bin and these were then added to get a total residual TS map for the full energy range. Our procedure revealed 43 new point source candidates (significance $\geq 4\sigma$) in the region of interest which are shown as green crosses in Fig. 1. We find multi-wavelength counterparts for

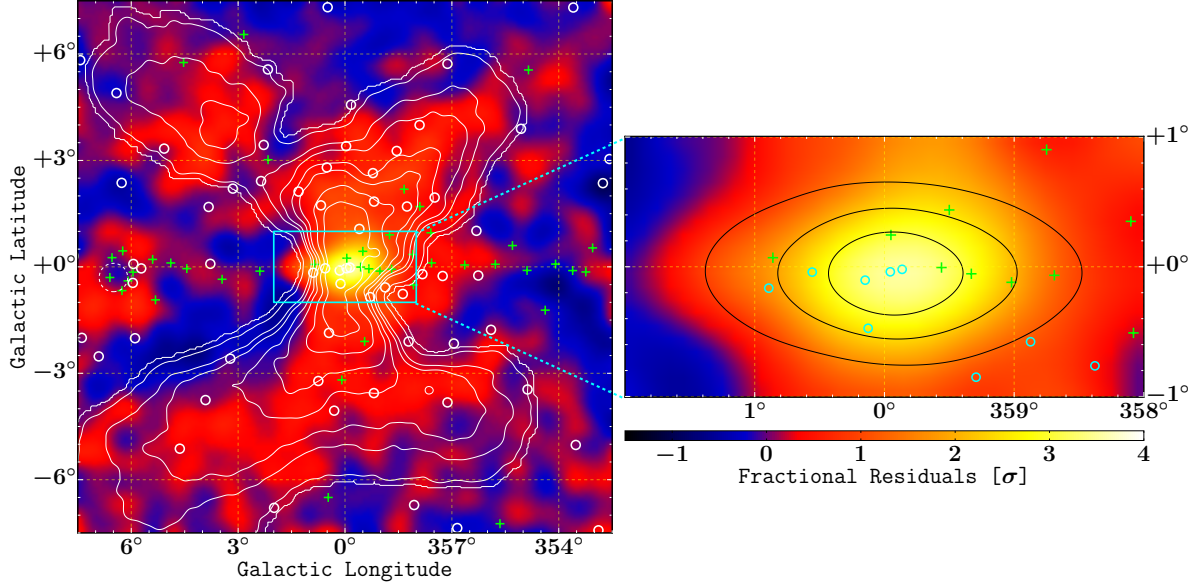


Figure 1: Residual map of the $15^\circ \times 15^\circ$ region of interest. Residuals are shown in units of $\sigma = (\text{counts} - \text{model})/\sqrt{\text{model}}$. Where the model includes previously-detected 3FGL (continuous circles) point sources [18], 43 additional point source candidates (green crosses), and the standard diffuse Galactic emission components related to the interstellar gas and radiation field. The white contours correspond to the X-bulge structure as seen by WISE [19, 20] in the infrared. A template based on the X-bulge was found to account for 17 ± 5 of the resolved point sources in the region of interest and was detected in the gamma-ray data at 21.1σ . The cluster of point sources on the Galactic plane at $l \approx 6^\circ$ may be associated with the W28 (white dashed circle) supernova remnant [9, 18]. The zoomed in region on the right shows the correlation with the near-infrared stellar density nuclear bulge data [21] (black contours). The X-bulge and nuclear bulge templates were included when the best fit parameters for the above model were found, but not when evaluating the above residuals. A Gaussian with radius 0.3° was used to smooth the images for display purposes.

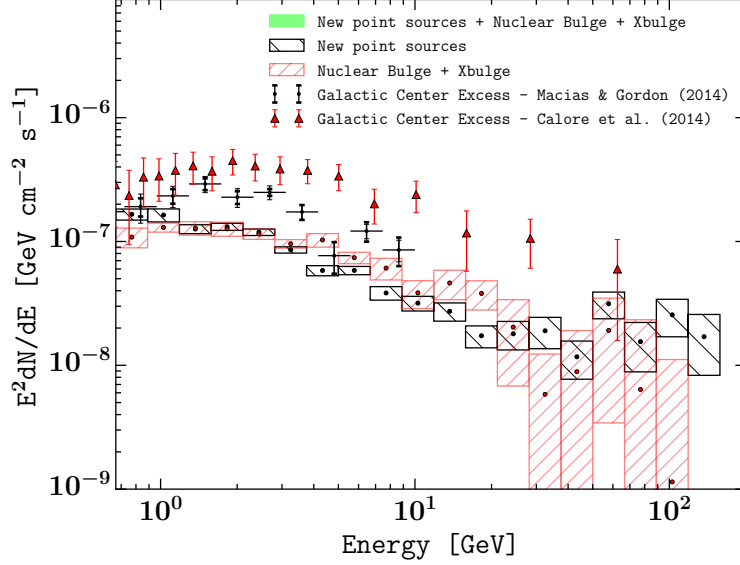


Figure 2: Differential flux of the new, statistically significant components in the Galactic Center. The black boxes are the combined spectrum of the 43 new point source candidates, red boxes are the superposition of the nuclear bulge and X-bulge differential fluxes, while the green boxes display the sum of these three components.

7 of our 43 point source candidates. Note that this does not preclude that the other 36 seeds are real sources since a considerable fraction of the Fermi-LAT sources [18] have no multi-wavelength associations.

Interstellar gas map templates constructed using the results of hydrodynamical simulations were found to be a better description of the diffuse γ -ray emission than the standard interpolation based maps. The log likelihood ratio was about 1237 which is better than a 35σ improvement. With this new diffuse Galactic emission model, we then proceeded to search for additional extended emission from the GC.

Extended gamma-ray emission in the GC need not be dark matter but may alternatively or additionally arise from unresolved sources connected to stellar populations. Almost half the stars [26] in the Galactic bulge are on orbits that contribute to the appearance (from the Earth) of an X-shaped over-concentration (the ‘X-bulge’) [27]. This structure has been particularly clearly revealed in a recent analysis [20] of 3.4 and 4.6 micron data collected by the WISE telescope. We investigated the relationship between the WISE and gamma-ray emission via maximum-likelihood ratio estimation with a flux normalized X-bulge template based on the average of the 3.4 and 4.6 micron data; the addition of an X-bulge template constructed from the micron data is favored by the gamma-ray data at about the 21σ level.

A further distinct stellar component within the wider Galactic bulge is the so-called nuclear bulge. This diskly distribution of stars concentrated within ~ 230 pc radius of the Galactic nucleus has experienced on-going star formation over the life of the Galaxy and represents $\sim 10\%$ of the overall bulge mass [28]. To determine whether the nuclear bulge is also correlated with the

GCE, we use a map constructed from a near-infrared stellar density measurement [21] and find a 13.6σ detection. In Fig. 1 we show the part of the data explained by X-bulge and nuclear bulge by subtracting them from our best fit model and then evaluating the residuals of the resultant model. As can be seen, the X-bulge and nuclear bulge are well traced by our residual gamma-ray maps. The correlation with the X-bulge is more evident away from the plane where the hard-to-model diffuse Galactic emission is no longer so dominant.

Best-fit spectral parameters were found using χ^2 fitting to the inferred flux points for energy bins. The X-bulge and nuclear bulge template had photon number (N) flux spectra (see Fig. 2) which, when fit with a power law in energy ($dN/dE \propto E^{-\Gamma}$), both had spectral slopes of $\Gamma = 2.4 \pm 0.1$, where here and in the rest of the article 68% confidence intervals are used. When we combine the X-bulge and nuclear bulge spectra, we find an exponential cut-off model ($dN/dE \propto E^{-\Gamma} \exp(-E/E_{\text{cut}})$) is preferred relative to a power law model at 4.0σ . The best fit spectral parameters were $\Gamma = 2.1 \pm 0.1$ and $E_{\text{cut}} = 13 \pm 4$ GeV. These are compatible with previous estimates of the GCE based on the square of an NFW template as well as with resolved MSPs and globular clusters containing MSPs [5].

Once the well-motivated and statistically-significant X-bulge and nuclear bulge templates are included, we find a dark matter component modeled with the square of an NFW spectrum (with an inner slope of 1.2) only has a 1.0σ detection which is well below the usual 4σ detection threshold. The 95% upper limit on this component's luminosity, for $E \geq 100$ MeV, was found to be 1.0×10^{37} erg/s. A dark matter NFW template constructed with an inner slope of 1.0 has an even lower significance.

The best fit luminosity of the combined X-bulge and nuclear bulge was found to be $(7.8 \pm 0.8) \times 10^{36}$ erg/s for $E \geq 100$ MeV where we adopted 8.25 kpc for the distance to the GC. We infer from ref. [29] that the stellar mass of the Galactic Bulge is 1.5×10^{10} solar masses (M_{\odot}), that the instantaneous stellar mass contributing to the appearance of the X-bulge over-density represents about 10% of this, $\sim 1.5 \times 10^9 M_{\odot}$, and that the nuclear bulge has a similar mass of $\sim 1.4 \times 10^9 M_{\odot}$. From these data we infer a $E \geq 100$ MeV luminosity-to-mass (LtM) ratio of $\sim 3 \times 10^{27}$ erg/s/ M_{\odot} for the combined structures. This lies between the LtM ratio we infer from ref. [30] for the MSP emission from the entire Milky Way of $\sim 2 \times 10^{27}$ erg/s/ M_{\odot} and the $\sim 5 \times 10^{28}$ erg/s/ M_{\odot} for globular cluster 47 Tuc (which has an MSP-dominated > 100 MeV luminosity of $(4.8 \pm 1.1) \times 10^{34}$ erg/s [31] and stellar mass of about $10^6 M_{\odot}$). Adopting the luminosity function of the resolved disk MSPs, $\sim 10^4$ unresolved MSPs [10] would be required to generate the combined X-bulge plus nuclear bulge luminosity.

Acknowledgements: RMC was the recipient of an Australian Research Council Future Fellowship (FT110100108). We thank Dustin Lang for making available code and data which helped with generating the X-bulge template and both Shogo Nishiyama and Kazuki Yasui for providing the data for the Nuclear bulge template. The authors would like to thank Felix Aharonian, Anthony M. Brown, Francesca Calore, Jean-Marc Casandjian, H. Thankful Cromartie, Seth Digel, Torsten Enßlin, Manoj Kaplinghat, Richard Tuffs, Ken Freeman, Ortwin Gerhard, Oleg Gnedin, Xiaoyuan Huang, David Nataf, Miles Winter, and Gabrijela Zaharijas for enlightening discussions.

References and Notes

- [1] L. Goodenough, D. Hooper, *ArXiv e-prints (arXiv:0910.2998)* (2009).
- [2] D. Hooper, T. Linden, *Phys. Rev.* **D84**, 123005 (2011).
- [3] K. N. Abazajian, M. Kaplinghat, *Phys. Rev.* **D86**, 083511 (2012).
- [4] C. Gordon, O. Macias, *Phys. Rev.* **D88**, 083521 (2013).
- [5] O. Macias, C. Gordon, *Phys. Rev.* **D89**, 063515 (2014).
- [6] K. N. Abazajian, N. Canac, S. Horiuchi, M. Kaplinghat, *Phys. Rev.* **D90**, 023526 (2014).
- [7] T. Daylan, *et al.*, *Phys. Dark Univ.* **12**, 1 (2016).
- [8] F. Calore, I. Cholis, C. Weniger, *J. Cosm. & Astropart. Phys.* **3**, 38 (2015).
- [9] M. Ajello, *et al.*, *Astrophys. J.* **819**, 44 (2016).
- [10] Q. Yuan, B. Zhang, *J. High Energy Astrophys.* **3**, 1 (2014).
- [11] R. M. O’Leary, M. D. Kistler, M. Kerr, J. Dexter, *ArXiv e-prints (arXiv:1504.02477)* (2015).
- [12] R.-Z. Yang, F. Aharonian, *Astron. & Astrophys.* **589**, A117 (2016).
- [13] X. Huang, T. Enlin, M. Selig, *J. Cosm. & Astropart. Phys.* **1604**, 030 (2016).
- [14] W. de Boer, I. Gebauer, A. Neumann, P. L. Biermann, *ArXiv e-prints (arXiv:1610.08926)* (2016).
- [15] F. Acero, *et al.*, *Astrophys. J. Supp.* **223**, 26 (2016).
- [16] M. Pohl, P. Englmaier, N. Bissantz, *Astrophys. J.* **677**, 283 (2008).
- [17] M. Ackermann, *et al.*, *Astrophys. J.* **750**, 3 (2012).
- [18] F. Acero, M. Ackermann, M. Ajello, A. Albert, *et al.*, *Astrophys. J. Supp.* **218**, 23 (2015).
- [19] E. L. Wright, *et al.*, *Astrophys. J.* **140**, 1868 (2010).
- [20] M. Ness, D. Lang, *Astrophys. J.* **152**, 14 (2016).
- [21] S. Nishiyama, *et al.*, *Astrophys. J. Lett.* **769**, L28 (2013).
- [22] Fermi science tools documentation, <http://fermi.gsfc.nasa.gov/ssc/data/analysis/documentation/>.
- [23] S. K. Lee, M. Lisanti, B. R. Safdi, T. R. Slatyer, W. Xue, *Phys. Rev. Lett.* **116**, 051103 (2016).
- [24] R. Bartels, S. Krishnamurthy, C. Weniger, *Phys. Rev. Lett.* **116**, 051102 (2016).

- [25] S. S. Wilks, *Ann. Math. Stat.* **9**, 60 (1938).
- [26] M. Portail, C. Wegg, O. Gerhard, *Mon. Not. R. Astron. Soc.* **450**, L66 (2015).
- [27] D. M. Nataf, A. Udalski, A. Gould, P. Fouqué, K. Z. Stanek, *Astrophys. J. Lett.* **721**, L28 (2010).
- [28] R. Launhardt, R. Zylka, P. G. Mezger, *Astron. & Astrophys.* **384**, 112 (2002).
- [29] J. Bland-Hawthorn, O. Gerhard, *Ann. Rev. Astron. & Astrophys.* **54**, 529 (2016).
- [30] M. Winter, G. Zaharijas, K. Bechtol, J. Vandenbroucke, *ArXiv e-prints (arXiv:1607.06390)* (2016).
- [31] A. A. Abdo, *et al.*, *Astron. & Astrophys.* **524**, A75 (2010).
- [32] A. W. Strong, *et al.*, Galprop version 54: Explanatory supplement, <http://galprop.stanford.edu>. Accessed: 2014-02-20.
- [33] P. M. W. Kalberla, *et al.*, *Astron. & Astrophys.* **440**, 775 (2005).
- [34] T. M. Dame, D. Hartmann, P. Thaddeus, *Astrophys. J.* **547**, 792 (2001).
- [35] T. Delahaye, A. Fiasson, M. Pohl, P. Salati, *Astron. Astrophys.* **531**, A37 (2011).
- [36] N. Bissantz, P. Englmaier, O. Gerhard, *Mon. Not. R. Astron. Soc.* **340**, 949 (2003).
- [37] D. J. Schlegel, D. P. Finkbeiner, M. Davis, *Astrophys. J.* **500**, 525 (1998).
- [38] M. Wolleben, *Astrophys. J.* **664**, 349 (2007).
- [39] O. Macias, C. Gordon, R. M. Crocker, S. Profumo, *Mon. Not. R. Astron. Soc.* **451**, 1833 (2015).
- [40] M. Ackermann, *et al.*, *Astrophys. J.* **793**, 64 (2014).
- [41] A. A. Abdo, *et al.*, *Astrophys. J.* **734**, 116 (2011).
- [42] G. Johannesson, E. Orlando, for the Fermi-LAT collaboration, *ArXiv e-prints (arXiv:1307.0197)* (2013).
- [43] M. Su, T. R. Slatyer, D. P. Finkbeiner, *Astrophys. J.* **724**, 1044 (2010).
- [44] F. Yusef-Zadeh, *et al.*, *Astrophys. J.* **762**, 33 (2013).
- [45] F. Aharonian, *et al.*, *Nature* **439**, 695 (2006).
- [46] C. J. Law, F. Yusef-Zadeh, W. D. Cotton, R. J. Maddalena, *Astrophys. J. Supp.* **177**, 255 (2008).

- [47] F. Acero, *et al.*, *Astrophys. J. Supp.* **223**, 26 (2016).
- [48] A. Albert, <http://www.mso.anu.edu.au/iau322/aalbert.pdf> (2016). IAU Symposium 322.
- [49] P. L. Nolan, *et al.*, *Astrophys. J. Supp.* **199**, 31 (2012).
- [50] R. N. Manchester, G. B. Hobbs, A. Teoh, M. Hobbs, *Astron. J.* **129**, 1993 (2005).
- [51] W. E. Harris, *Astron. J.* **112**, 1487 (1996).
- [52] D. A. Green, *Bull. Astron. Soc. India* **42**, 47 (2014).

Appendix

Observations

We examined ~ 7 years of Fermi-LAT data (August 4, 2008–September 4, 2015) selecting PASS 8 ULTRACLEANVETO¹ class events with energies between 667 MeV–158 GeV. Compared to previous LAT data releases, PASS 8 provides greater acceptance and improved energy measurements. The selected events class has the most robust cuts on residual cosmic-ray emission contamination.

We extracted Fermi-LAT data within a square region of $15^\circ \times 15^\circ$ centered at Galactic coordinates $(l, b) = (0, 0)$ and made no distinction between *Front* and *Back* events. To avoid contamination from terrestrial γ -rays, only events with zenith angles smaller than 90° were used. The Fermi Science Tools v10r0p5 were used for this analysis.

Templates

The Galactic diffuse γ -rays resulting from the interaction of cosmic-ray electrons and protons with the interstellar gas and radiation field were modeled with a similar method [15] as that used for the 3FGL catalog [18]. We fitted a linear combination of atomic and molecular hydrogen gas templates, an IC map cube as obtained with GALPROP [32], specialized templates for the *Sun* and the *Moon*, an isotropic component², and a model for the γ -ray emission associated with Loop I.

The atomic and molecular hydrogen gas column densities were each distributed within four Galactocentric annuli to account for the non-uniform cosmic-ray flux in the Galaxy. In the following subsections, we describe the construction of these templates.

We do not include the empirically-derived extended emission templates used by the Fermi-Collaboration when generating their most recent version of diffuse galactic emission model [15], because they were used to flatten residuals over larger regions of the sky than we are interested in this analysis and they are specifically constructed in support of the generation of the *Fermi*-LAT point-source catalogs.

¹http://fermi.gsfc.nasa.gov/ssc/data/analysis/documentation/Pass8_usage.html

²`iso_P8R2_ULTRACLEANVETO_V6_v06.txt`

HI and H₂ Gas Column Density Templates

We investigate two different methods for constructing the gas map templates:

1. **Interpolation approach:** this method has been used to produce the interstellar gas distribution models employed in most previous analyses of the GCE and is the standard approach employed in GALPROP and by the Fermi team.

In the interpolation approach, the gas column density maps are produced using the method given in Appendix B of ref. [17]. Atomic hydrogen column density is derived from the 21 cm LAB survey of Galactic HI [33]. Molecular hydrogen is traced by the 2.6 mm emission line of carbon monoxide (CO) from the 115 GHz Center for Astrophysics survey of CO [34]. The emission maps are decomposed into Galactocentric annuli via the relation,

$$V_{\text{LSR}} = \left(V(R) \frac{R_{\odot}}{R} - V(R_{\odot}) \right) \sin(l) \cos(b), \quad (1)$$

where V_{LSR} is the radial velocity, relative to the local standard of rest, of the gas at Galactocentric radius R with orbital velocity $V(R)$ observed in the direction (l, b) and R_{\odot} is the distance of the Sun to the Galactic Center. We assumed a spin temperature of $T_S = 170$ K throughout the Galaxy and $R_{\odot} = 8.25$ kpc. We checked that our results did not significantly change when we used other reasonable values such as $T_S = 150$ K and $R_{\odot} = 8$ kpc.

In our region of interest, the annuli decomposition interpolation method does not produce a reliable map of the gas column density as kinematic resolution is lost near $l = 0^\circ$. In the interpolation approach, the gas column density in the region $|l| < 10^\circ$ was estimated by interpolating within each annulus from the boundaries. Values at the boundaries of the interpolated region were chosen as the mean gas column density within a range of $\Delta l = 5^\circ$ on both sides of the boundary. Each pixel in the interpolated region was then renormalized to preserve the total gas column density in each line of sight.

2. **Hydrodynamic approach:** this method was pioneered by Pohl et al. [16]. See also ref. [35] for discussion regarding the construction of the HI map. The hydrodynamic approach introduces a probabilistic deconvolution method for assigning gas clouds to distances via simulated gas flow model predictions. The Pohl et al. interstellar gas flow model follows hydrodynamic simulations inside the solar circle outlined in ref. [36], taking the spiral arms and Galactic bar into account. The presence of non-circular motion in the inner Galaxy provides kinematic resolution towards the GC. As we used 8.25 kpc for our distance to the GC, the distances were scaled to account for the 8 kpc solar circle in the simulation. We converted the line intensities of the Pohl et al. interstellar gas flow model to Galactocentric annuli column density maps. Outside the solar circle, pure circular motion with velocities described by equation (1), was assumed with an additional correction for the motion of the Sun relative to the local standard of rest. This meant there was lack of CO and HI gas placed in the outer annuli. We corrected for this by interpolating the outer annuli pixels in the line-of-sight maps which have $|l| < 15^\circ$ and then renormalized each pixel to preserve the total gas column density in each line of sight. For CO we interpolated beyond 10 kpc and for HI we interpolated beyond 8 kpc from the GC.

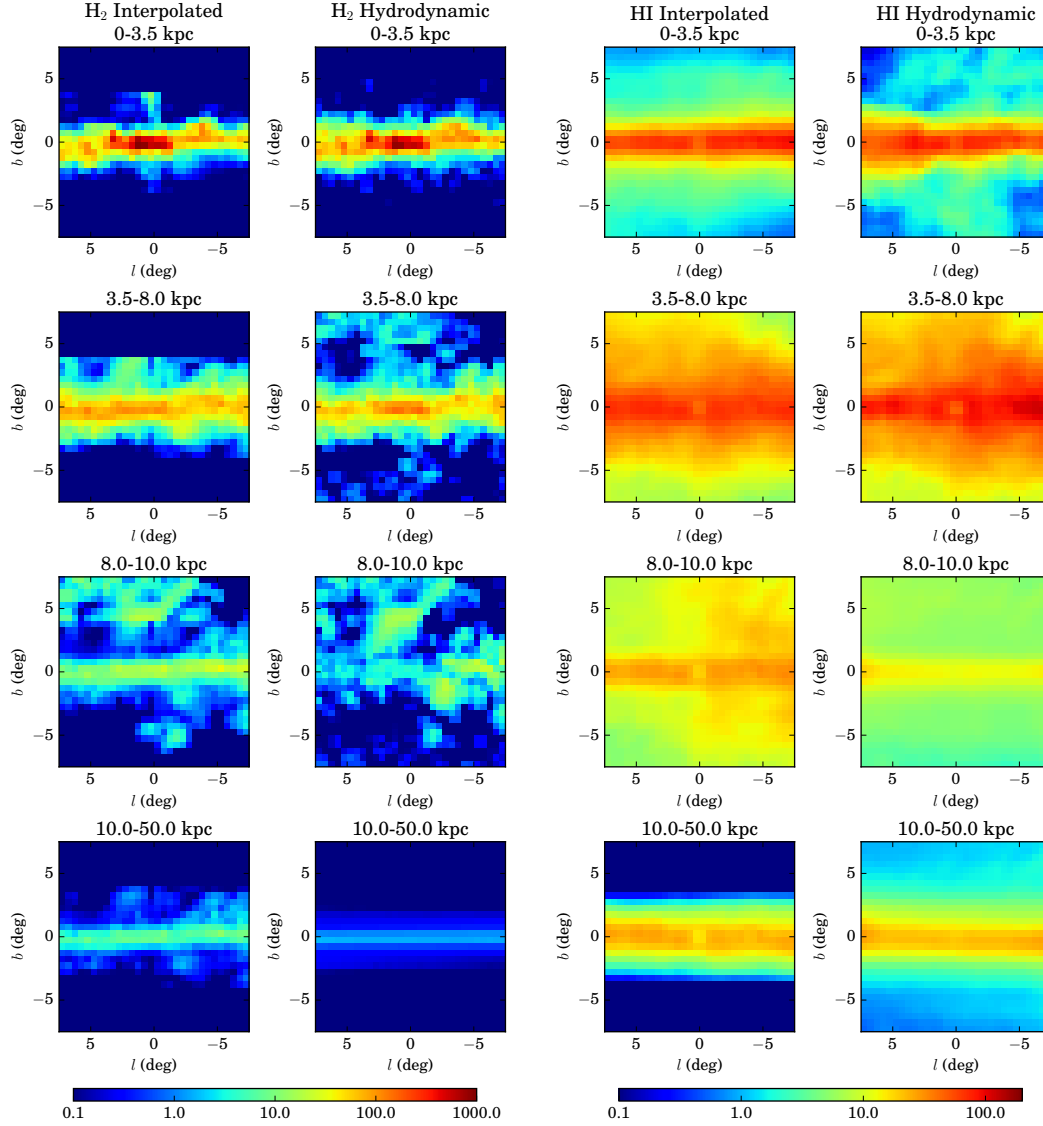


Figure 3: Column density maps for the interpolated and hydrodynamic methods. The minimum and maximum radii of each annulus is listed. The units for the H_2 proportional CO maps are $\text{K}\cdot\text{km/s}$. The units for the HI maps are 10^{20}cm^{-2} .

The results of the two methods are compared in Fig. 3.

Dust Correction Templates

Molecular hydrogen that is not well mixed with carbon monoxide will not be traced by the CO 2.6 mm emission. Furthermore, assuming a constant atomic hydrogen spin temperature $T_S = 170\text{ K}$ can give an incorrect estimate of column density as the spin temperature can vary along a line of

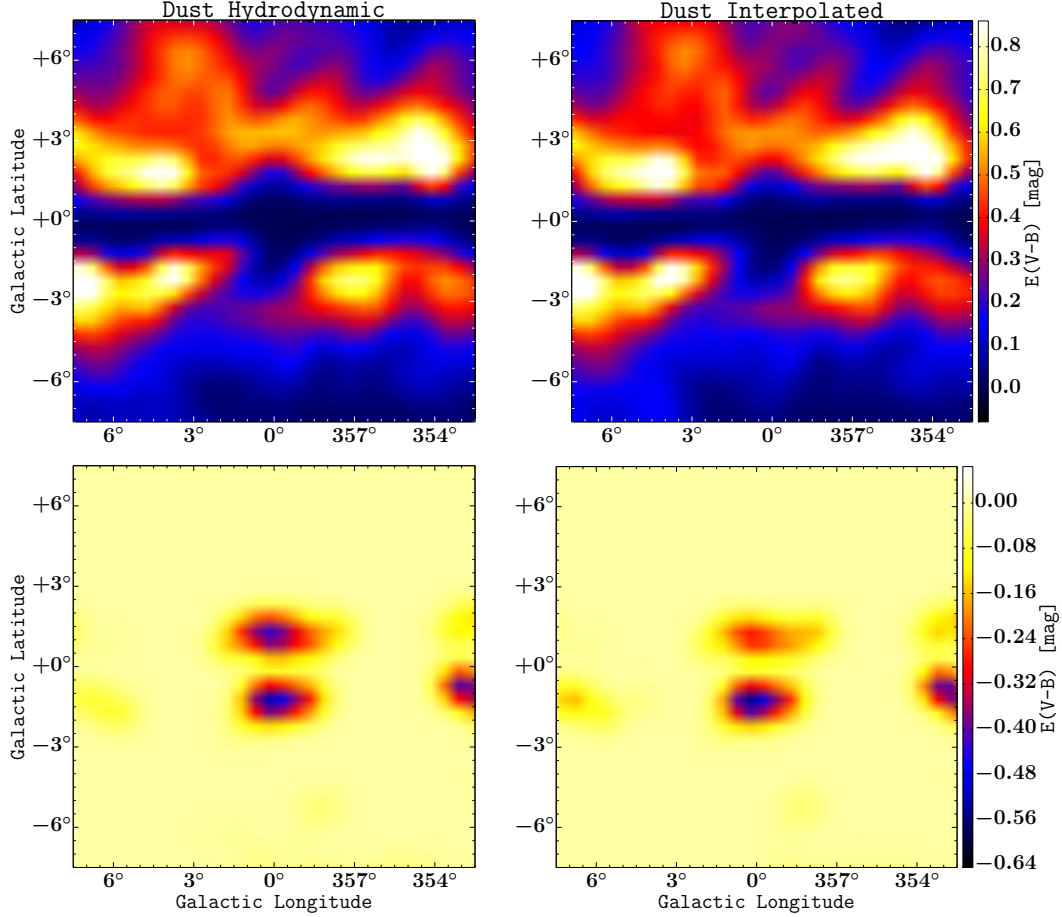


Figure 4: Top: Dark neutral medium maps. Bottom: HI correction maps. The left (right) hand side maps were based on fitting the hydrodynamic (interpolated) HI and CO maps with the $E(B-V)$ dust map. For display purposes a smoothing with a Gaussian with a radius of one degree was performed.

sight. To correct for these deficiencies we included dust templates based on the methods used in ref. [17]. Infrared thermal emission from dust provides an alternative method of tracing hydrogen gas in the Milky Way. The correction templates are obtained by subtracting the components of the dust emission that are correlated with the gas already traced by 21 cm and 2.66 mm emission.

We applied this method to $E(B-V)$ maps of ref. [37]. Regions that are densely populated by infrared point sources (or potentially a collection of unresolved point sources) could contaminate the $E(B-V)$ map, resulting in an over estimation of the dust column density. To mitigate this, we apply a magnitude cut of 5 mag to the $E(B-V)$ maps. After subtracting the components of the $E(B-V)$ map that were linearly correlated with the hydrogen gas maps, the residuals were separated into positive and negative components. The positive residuals physically represent hydrogen that is not traced by the relevant emission, know as the dark neutral medium, or an over estimation of the atomic hydrogen spin temperature. Negative residuals represent an underestimation of the spin temperature. The results are displayed in Fig. 4. We also tried using a magnitude cut of 2 mag

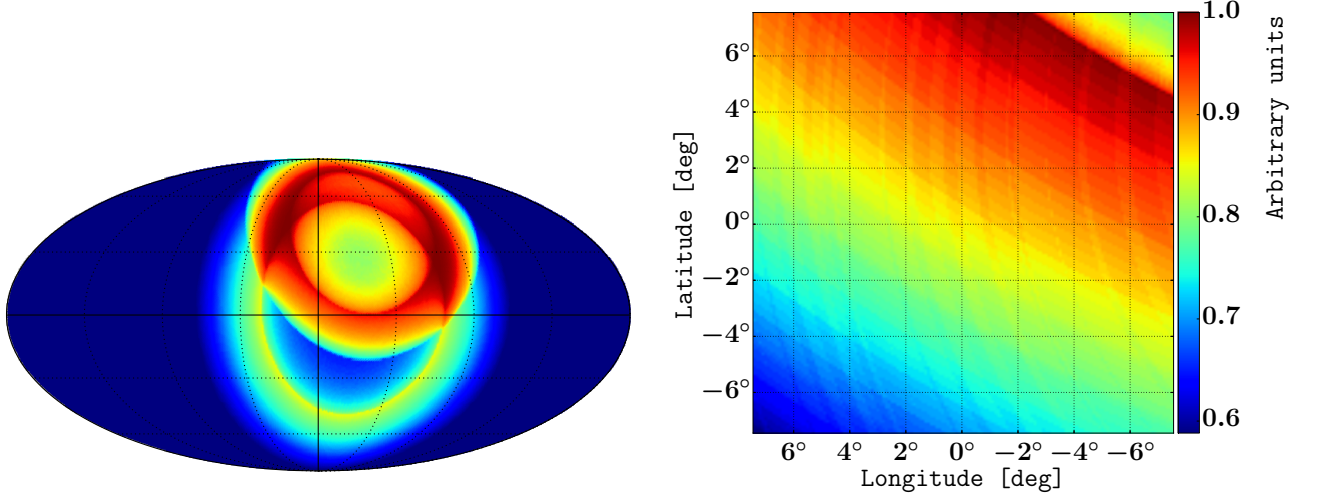


Figure 5: Loop I template adapted from ref. [38]. A histogram equalized color mapping is used for display. The map is appropriately normalized, in our region of interest, for analysis with the *Fermi* Science Tools. On the left we show a full sky version of the map and on the right a we have zoomed in to our region of interest.

and found it did not significantly change our results.

Inverse Compton Emission Template

Whereas the bremsstrahlung and π^0 -decay components can be adequately described by the gas maps described above, there is no analogous empirical template for the Galactic IC emission. We use the GALPROP package v54.1 [32] to generate such a template. The authors of ref. [17] did a comprehensive comparison of 128 different GALPROP models with all sky Fermi-LAT data. They found a range of possible values for the input GALPROP parameters that are consistent with γ -ray and local measurements of cosmic-ray data. In this work, we consider the IC template generated with GALDEF file

galdef_54_Lorimer_z10kpc_R20kpc_Ts150K_EBV2mag³ as our reference model. The IC component is of much smaller intensity compared to the interstellar gas diffuse Galactic emission components. Our results were not changed significantly when using alternative IC templates from ref. [17].

Loop I Template

Loop I is a bright, large angular scale, non-thermal structure. Obtaining a precise template of this source is not possible since its γ -ray emission is not well traced by radio emission. We note that the standard diffuse Galactic emission used in our previous investigations of the GCE [4, 5, 39]

³<http://galprop.stanford.edu/PaperIISuppMaterial/>

employed a uniform-patch Loop I template whose shape was derived by visual inspection of the γ -ray residuals. Following the same approach taken in recent studies by the Fermi Collaboration [40], in this work we used a geometrical template proposed by ref. [38] which is based on a polarization survey at 1.4 GHz (see Fig. 5). We adopted the same morphological parameters for the shells assumed in ref. [40].

Sun and Moon emission Templates

Cosmic-ray e^\pm interacting through IC scattering with the solar radiation field and solar atmosphere produce extended γ -ray emission from around the Sun [41]. Furthermore, cosmic-ray interactions taking place in the lunar lithosphere make the Moon appear as a reasonably bright extended γ -ray source and the Moon moves through a large fraction of the sky. In order to account for the diffuse emission from these objects, we construct specialized templates for our region of interest by making use of the *gtsuntemp* [42] tool.

New Templates

X-bulge

We followed a procedure based on the method described in ref. [20]. We used the 3.4 (W1) and 4.6 (W2) micron WISE data masking out the top and bottom 5% of pixels based on W1–W2 color, as well as pixels with negative flux. We then subtracted a best fit exponential disk model from W1 and W2 where the disk amplitude was allowed to be different for the W1 and W2 bands:

$$\text{bulge} \propto \exp \left(- \frac{\sqrt{\left(\frac{(b-b_0) \cos(\theta) + (l-l_0) \sin(\theta)}{\beta} \right)^2 + [(l-l_0) \cos(\theta) - (b-b_0) \sin(\theta)]^2}}{(\alpha/8.25\text{kpc})(180/\pi)} \right) \quad (2)$$

where $\alpha = 1.2$ kpc, $\beta = 0.35$, $l_0 = -0.45^\circ$, and $b_0 = 0.11^\circ$. We then performed a 50 pixel (1.7°) median filter of masked residuals (median of unmasked pixels) on both exponential subtracted maps. To make our template for comparison with the Fermi-LAT data, all pixels values below zero were set to zero in each median filtered exponential subtracted map and our template was then constructed by taking the average of the two resultant maps. The resulting template is displayed in Fig. 6.

Nuclear Bulge

We used a map constructed from a near-infrared stellar density measurement of the central region of our Galaxy ($|l| \geq 3^\circ$ and $|b| \geq 1^\circ$) and subtracted a best fit Galactic disk component [21]. In order to remove artificial sharp boundaries in the map, induced by survey patches, all pixels below $15 \text{ stars/arcmin}^2$ were set to zero. The resulting template is displayed in Fig. 7.

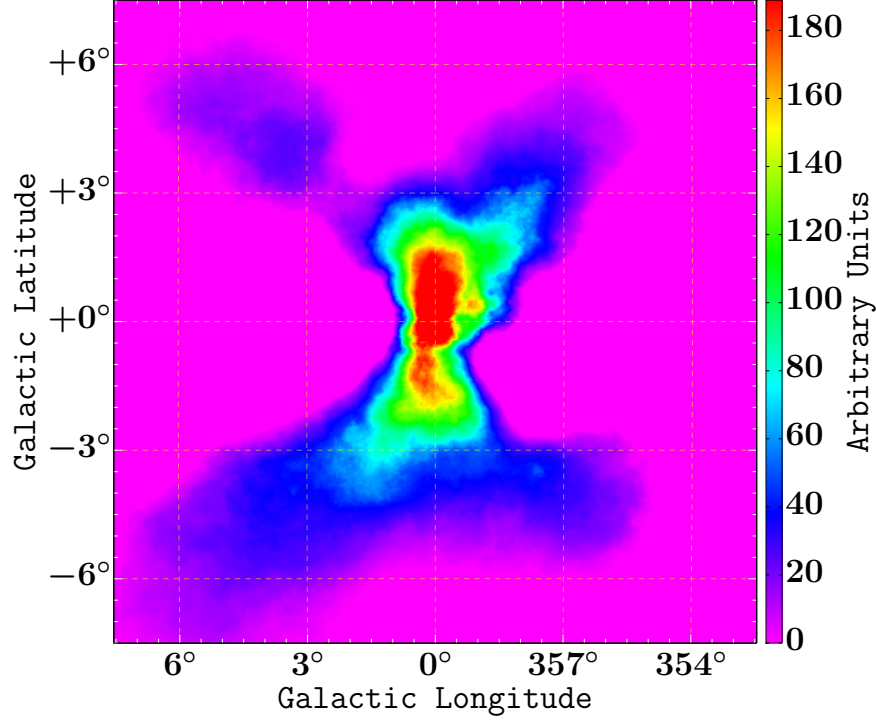


Figure 6: The X-bulge template based on the smoothed W1 and W2 WISE data [20] with a best fit exponential bulge component subtracted.

Dark Matter

We used a physical model that has been shown by previous works to describe well the GCE [1, 2, 3, 4, 5, 6, 7, 8, 9], namely a generalized NFW density profile:

$$\rho(r) = \frac{\rho_{\odot}}{\left(\frac{r}{R_{\odot}}\right)^{\gamma} \left(\frac{1+r/R_s}{1+R_{\odot}/R_s}\right)^{3-\gamma}}, \quad (3)$$

where R_{\odot} is the Sun's distance from the GC, ρ_{\odot} is the dark matter density at R_{\odot} , R_s is the scale radius of the Galaxy's dark matter halo, and γ is the profile slope. We use standard values for these parameters to $R_s = 23.1$ kpc, $R_{\odot} = 8.25$ kpc and $\rho_{\odot} = 0.36$ GeV/cm³, $\gamma = 1.2$ [4]. We found our results were not qualitatively changed if we instead used the canonical $\gamma = 1$ value. The square of an NFW density profile (NFW²) is representative of a tentative annihilating dark matter signal in the GC. Alternatively, it could also represent an unresolved population of Galactic bulge MSPs [3, 5, 10].

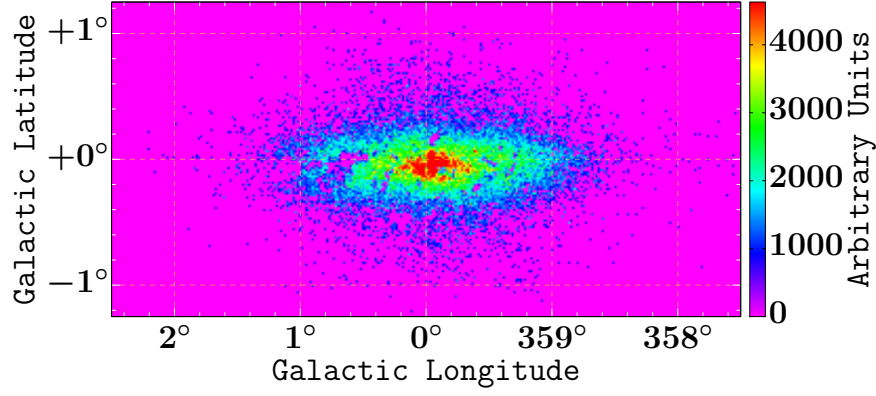


Figure 7: The nuclear bulge template based on data from ref. [21] with a best fit exponential disk component subtracted.

Alternative Explanations

Fermi Bubbles

The Fermi Bubbles [40, 43] (FB) are giant lobes that extend up to ~ 7 kpc from the Galactic plane into both the North and South Galactic hemispheres. Recently, Acero et al. [15] performed a morphological study of these structures in the inner 20° of the GC. They found that the boundaries of the Fermi bubbles are well described by two catenary curves of the form $10.5^\circ \times (\cosh((l - 1^\circ)/10.5^\circ) - 1^\circ)$ and $8.7^\circ \times (\cosh((l + 1.7^\circ)/8.7^\circ) - 1^\circ)$ for the Northern and the Southern bubbles, respectively. However, the catenary geometry does not match the X-shaped excess we see in our residual and TS maps in Figs. 1 and 8. We found the addition of a catenary template did not qualitatively affect our results. As this template had a low TS value we did not include it in our final results.

In ref. [40], the spectrum of the Fermi bubbles was determined from the residuals in the energy range between 0.7 GeV and 10 GeV. They examined an area near the southern edge of the Fermi bubbles ($55^\circ < b < 40^\circ$ and $15^\circ < l < 15^\circ$). A power-law fit in this region had a spectral index index 1.9. In contrast, we found our X-bulge, for the same energy range, had a power-law fit with a significantly softer spectral index of 2.34 ± 0.05 . Also, we estimate that the X-bulge plus nuclear bulge has a solid angle of 0.03 sr. Therefore it has a luminosity per solid angle of $(2.7 \pm 0.3) \times 10^{38}$ erg/s/sr. While the Fermi bubbles, for $|b| \geq 10^\circ$, have a solid angle of about 0.7 sr and a luminosity per solid angle of $(6.3 \pm 0.1) \times 10^{37}$ erg/s/sr [40]. Even taking a wide range of systematic effects into account, the highest luminosity per solid angle for the Fermi bubbles was only 8.6×10^{37} erg/s/sr [40]. In summary, current spatial and spectral evidence seems to disfavor a Fermi-bubbles explanation for the X-bulge emission.

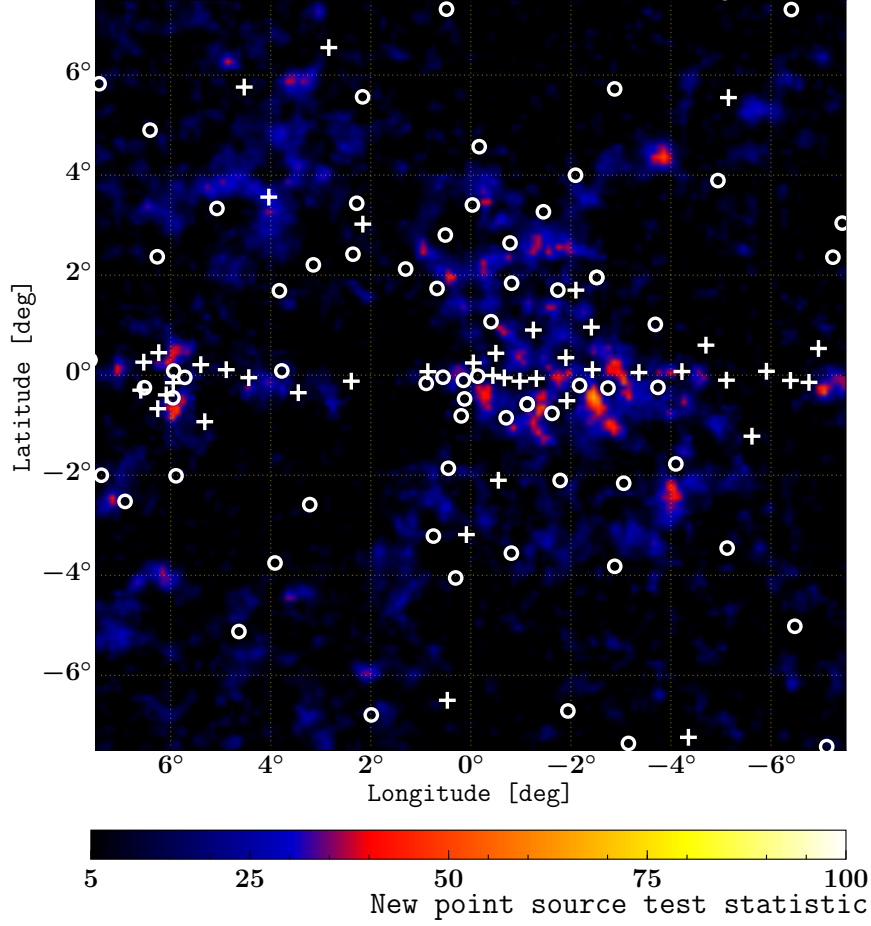


Figure 8: Significance map of the $15^\circ \times 15^\circ$ region about the GC output from `gttsmap` after the new point sources have been identified. The energy range shown is 667 MeV–158 GeV. The 3FGL point sources (white circles) and the new point sources (white crosses) are displayed. Table 1 and 2 summarize the basic properties of the new point sources.

Galactic Ridge Cosmic Rays

A recent study [5] carried out a Fermi-LAT analysis of the Galactic ridge region ($2^\circ \times 1^\circ$ around the GC) using templates obtained from measurements at other wavelengths. Either a 20-cm map [44] or a HESS residuals [45] map was used with similar results. The 20-cm template was based on Green Bank Telescope continuum emission data which measures non-thermal and thermal plasma distributions [46].

We found this map could be used to replace the nuclear bulge template with a similar level of significance and spectrum. Therefore there is systematic uncertainty surrounding the fractional contribution of cosmic rays to the nuclear bulge. Compatible ranges of cosmic ray contribution are consistent with current models [39].

Bin-by-Bin Analysis

Following previous work [9, 47, 48], we employed a bin-by-bin analysis technique, in which we split the Fermi-LAT data into 19 logarithmically spaced energy bins. Within each energy bin we performed a separate maximum-likelihood fit [18] with the *pyLikelihood* analysis tool⁴. The bin size was chosen to be larger than the LAT energy resolution, but narrow enough that the Galactic emission spectral components can be simply approximated by a power law model. We note that this bin-by-bin method means a parametric form of the spectrum of the sources does not have to be chosen prior to the fit. The bin-by-bin method also significantly decreases the number of iterations required to reach convergence in this very challenging region of interest.

Once the bin-by-bin method had converged, the inferred spectrum of each source was either fitted by a power law or exponential cut-off model. Only spectral bins which had $TS \geq 1$ were used. The errors from the bin-by-bin fit were added in quadrature to the systematic errors caused by the uncertainties in the effective area [18]. These effective area errors were taken to be f_i^{rel} times the predicted flux for bin i . Where f_i^{rel} is interpolated from the values given in ref. [18]. The spectrum was modeled by an exponential cutoff if

$$TS_{\text{curvature}} \equiv -2 (\log \mathcal{L}(\text{exp. cut-off}) - \log \mathcal{L}(\text{power law})) \geq 16$$

where $\mathcal{L}(i)$ is the maximum likelihood value for model i .

Comparing Hydrodynamic and Interpolated Gas Templates

Initially we fit the LAT data with a model comprised of the 3FGL [18] point sources present in our region of interest plus four other spatially extended sources (HESS J1825-137, RX J1713.7-3946, W28 and W30) reported by the Fermi-LAT team.

To identify the most suitable gas templates for our study, we performed a scan in which we evaluated the improvement of the likelihood fit to the region of interest when the gas maps used were the ones created with the interpolation method or the hydrodynamical method. Figure 9 shows that the data preferred the hydrodynamical method.

During optimization, the flux normalization of the 3FGL sources were left free in each energy bin. We also simultaneously fit the 13 diffuse components' (HI annuli, CO annuli, dust templates, Loop I, inverse Compton, and isotropic) normalizations but kept the *Sun* and *Moon* fluxes fixed to their nominal values.

Point Source Search

In order to search for missing point sources we divided the region of interest in $0.1^\circ \times 0.1^\circ$ grid positions and examined the significance of a trial point source with a power-law spectrum, with a fixed slope of two, at the center of each pixel while keeping all other components fixed. The outcome of this was a residual test statistic (TS) map (the `gttsmap` utility was used for this step).

⁴<http://fermi.gsfc.nasa.gov/ssc/data/analysis/documentation/>

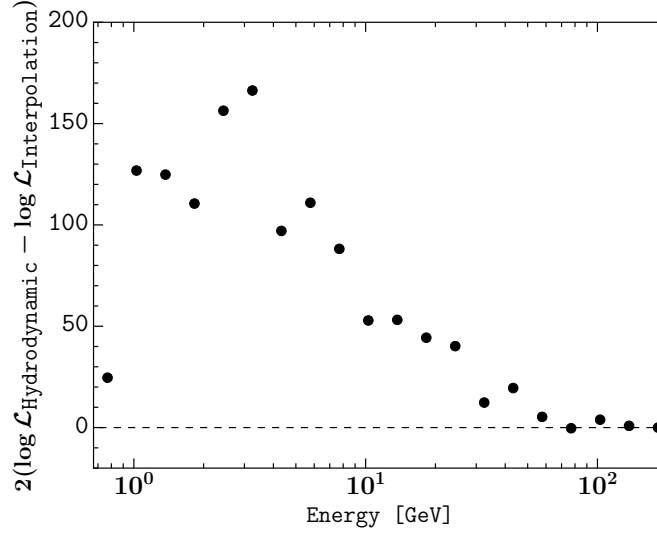


Figure 9: Comparison of the log-likelihood obtained for two different interstellar gas models: Hydrodynamic [16] gas maps vs the interpolation ones used in the standard Galactic diffuse emission model. Summing over the energy bins gives $\text{TS}_{\text{Hydrodynamic}} = 1237$.

In accordance with our bin-by-bin method, a residual TS map was computed for each energy bin and these were then added to get a total residual map for the full energy range.

From the total residual TS map we generated a list of all the pixel clusters with TS values above the detection threshold that looked reasonably isolated under visual inspection. The coordinates of the source candidates were calculated as the average of adjacent pixel positions weighted by their respective TS values [49]. We then added the seeds to our model and reran the bin-by-bin analysis routine where all components including the new point source were simultaneously fitted. Note that in the thresholding pass, convergence was achieved by adding the point source seeds to the model consecutively in order of decreasing TS. This made the method more robust against source confusion. We did not use *gtfindsrc* to refine the seeds' positions because it is based on an unbinned likelihood method [49]. When doing a global analysis, as opposed to a bin-by-bin analysis, each new point source candidate has two degrees of freedom for the power law and two degrees of freedom for its position. In that case a $\text{TS} \geq 25$ (which corresponds to 4σ) is used as the detection condition [18]. However, since we used a bin-by-bin analysis with 19 energy bands in which the point source amplitude was allowed to vary, we used a threshold of $\text{TS} \geq 55$ which for 21 degrees of freedom also corresponds to a 4σ detection [25]. All new point sources that were found to have a $\text{TS} \geq 55$ were allowed to remain in our baseline model. We iterated through these steps until no more seeds which gave $\text{TS} \geq 55$ were found.

The total set of new point sources found in this work are displayed in Fig. 8 along with the TS residual map obtained in our last iteration. Although the model including all the new point sources is a much better representation of the region of interest, a few hot spots still remain. These are, however, found to be below the detection threshold of $\text{TS} \geq 55$ in the maximum likelihood step. As can be seen from Fig. 8, the X-bulge morphology is clearly visible in the residual TS values.

To identify possible multi-wavelength counterparts to the gamma-ray sources we searched in the seed locations within the 68% containment of the point spread function for one of our highest energy bands $\sim 0.1^\circ$ – around each source in the ATNF pulsar [50], globular cluster [51] and supernova remnant (SNR) [52] catalogs for potential gamma-ray emitters. We found spatial overlaps for 7 of our 43 point source candidates (see Tables 1 and 2). Note that this does not preclude the possibility that the other 36 seeds are real sources since a considerable fraction of the Fermi-LAT sources [18] have no multi-wavelength associations.

Search for Extended Emission

We first examined the case in which the set of new point sources (Table 1) is not included in the model. We fitted for extended excess γ -ray emission with our bin-by-bin method to derive fluxes that are independent of the choice of spectral model. Within each bin, the spectrum of the NFW² source and the included point sources and included extended templates were modeled as power laws with fixed spectral index of two. Due to the small size of our bins, our results were not sensitive to the precise spectral index used. In each energy bin, the amplitudes of all included point sources and all included extended templates were simultaneously fit along with the NFW² amplitude for that bin. This allowed us to effectively marginalize over the statistical uncertainties in these other sources. As there are 19 degrees of freedom in this case, we used a 4σ detection threshold of $TS \geq 53$.

The top panels of Fig. 10 show that if we used the interpolated gas maps without including any new point sources, we were able to reproduce the results of previous studies (e.g., [3, 4, 5, 6, 7, 8, 9]), while the bottom panels show that once we used our new gas maps, included our new point sources and our new extended templates for the X-bulge and nuclear bulge, the fitted dark matter amplitude is negligible in every energy bin.

The contributions of the different components for our proposed model of the Galactic Center excess are shown in Fig. 11. The values for our combined X-bulge and nuclear bulge spectrum are given in Table 3. Our inferred molecular-hydrogen-to-CO conversion factor (X_{CO}) is shown in Table 4 and is consistent with the results from all sky fits [17]. As in ref. [15] we evaluated X_{CO} using our 2 GeV energy bin fit results. The last annuli has large errors for X_{CO} and so we don't list the value for that one.

We found most of our results were not sensitive to changing the number of annuli to five by splitting our first annuli into two annuli with radii 0 to 1.5 kpc and 1.5 to 3.5 kpc. However, we got unrealistic X_{CO} values for the innermost annuli in that case. Therefore, we stuck to the four annuli case shown in Fig. 3. Note that we did not explicitly use the X_{CO} values in performing our fits and we are only quoting their inferred values to demonstrate the fitted amplitudes for our interstellar gas maps are consistent with previous results.

Determining the X-bulge Contribution to the Resolved MSPs

The 3FGL and new point sources may have contributions from a number of sources such as the X-bulge, the nuclear bulge, the Galactic disk, extragalactic sources, and some may be small scale

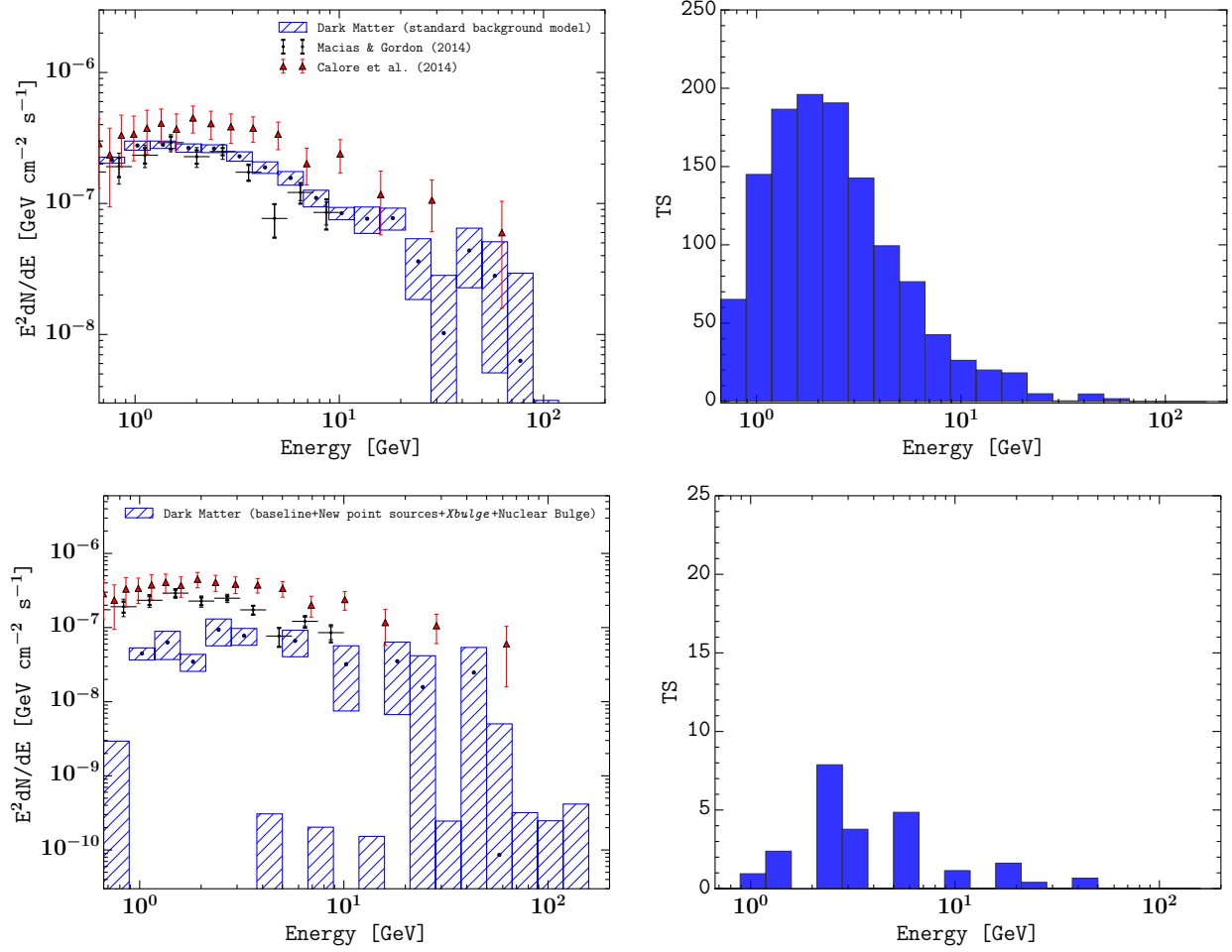


Figure 10: Top: Replication of previous results. In the left panel the dark matter energy spectrum as extracted from the $15^\circ \times 15^\circ$ around the GC assuming a generalized NFW² profile with an inner slope $\gamma = 1.2$. In the right panel the TS values obtained at each energy bin for the extended NFW² source are shown. In the top panels we used the interpolated gas maps and did not include any new point or extended sources. We found a total $TS_{\text{NFW}^2} = 1220$ for the NFW² source. With 19 degrees of freedom, this corresponds to a 33σ detection of dark matter, consistent with previous studies. Bottom: our new analysis where the hydrodynamic gas maps, new point sources and new extended X-bulge and nuclear bulge templates are included. The significance of the NFW² model has reduced to 1.0σ .

corrections to the diffuse Galactic emission model [9, 18]. We modeled the probability of a point source being resolved in pixel i as a Poisson distribution with mean

$$\mu_i = \mu_{\text{Xbulge}} \text{Xbulge}(l_i, b_i) + \mu_{\text{isotropic}} + \mu_{\text{exp}} e^{-|b_i|/\beta}$$

where $\text{Xbulge}(l_i, b_i)$ is the value of the X-bulge template at pixel i . To determine the values of μ_{Xbulge} , $\mu_{\text{isotropic}}$, μ_{exp} , and β , we maximized the likelihood which is given by

$$\mathcal{L} = \prod_{i \in \text{point source}} \mu_i e^{-\mu_i} \times \prod_{i \notin \text{point source}} e^{-\mu_i}$$

where the products are over pixels with and without point sources. The contribution of the X-bulge for a point source at pixel i is given by $\mu_{\text{Xbulge}} \text{Xbulge}(l_i, b_i) / \mu_i$ and is listed in Tables 2 and 5.

Over the entire region of interest, the X-bulge contribution to the resolved point sources was $\sum_i \mu_{\text{Xbulge}} \text{Xbulge}(l_i, b_i) / \sum_i \mu_i = 0.16 \pm 0.05$. We can estimate the total number of point sources attributable to the X-bulge by multiplying this quantity with the total number of resolved point sources in our region of interest. The scale height, of the exponential disk, was found to be $\beta = (34 \pm 6)$ pc which is compatible with the scale height of the nuclear stellar disk component of the nuclear bulge [21].

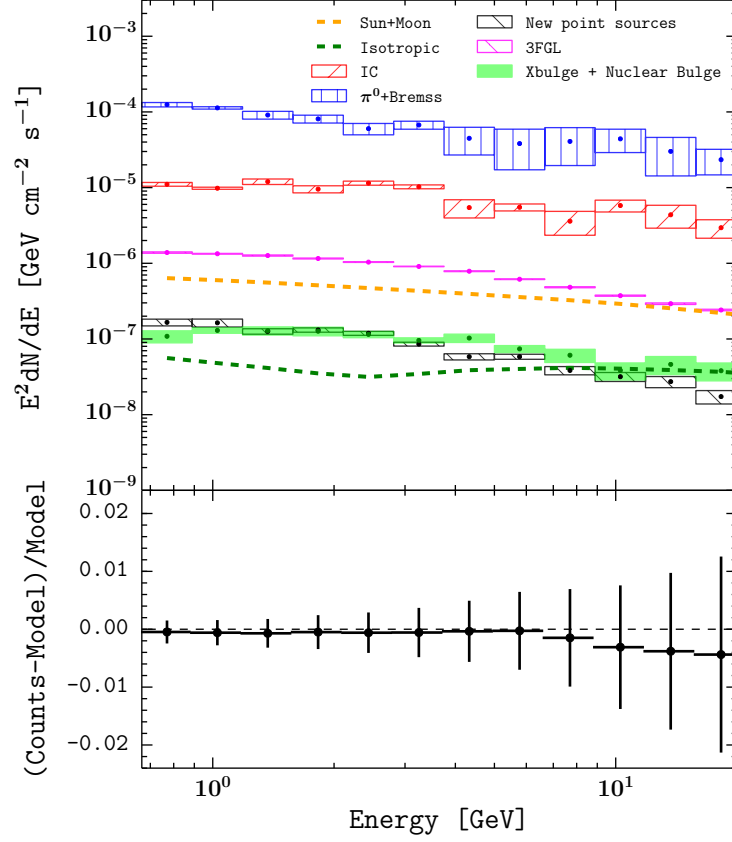


Figure 11: Top: Differential flux of the different components in the $15^\circ \times 15^\circ$ region about the Galactic Center. The model considered in the fit is the *baseline+NP+nuclear bulge+X-bulge* model. To reduce clutter the spectrum of the combined H I and CO gas maps are shown. The box heights represent the the 68% C.I. regions. Bottom: spectral residuals associated with the fit and determined from the full region of interest.

Name	l [deg]	b [deg]	Association or spatial overlap
FGC J1756.0 -2508	4.44	-0.049	1FIG J1755.5-2511
FGC J1801.3 -2449	5.32	-0.93	1FIG J1801.2-2451, PSR J1801-2451 [50]
FGC J1744.2 -2932	359.33	-0.054	1FIG J1744.2-2930
FGC J1739.6 -3022	358.1	0.35	1FIG J1739.4-3010, PSR J1739-3023 [50]
FGC J1735.9 -3028	357.59	0.96	1FIG J1735.4-3030, Terzan 1 [51]
FGC J1737.2 -3145	356.64	0.053	1FIG J1737.4-3144
FGC J1734.9 -3228	355.78	0.073	1FIG J1734.6-3228
FGC J1731.6 -3235	355.3	0.6	1FIG J1731.3-3235
FGC J1729.1 -3443	353.24	-0.144	1FIG J1728.6-3433
FGC J1736.5 -3420	354.38	-1.22	1FIG J1736.1-3422
FGC J1759.7 -2353	5.95	-0.15	
FGC J1758.1 -2320	6.24	0.45	
FGC J1727.7 -2302	2.84	6.55	
FGC J1711.3 -3008	354.85	5.55	
FGC J1733.1 -2910	358.34	2.19	
FGC J1805.1 -3619	355.65	-7.24	
FGC J1734.6 -2202	4.531	5.76	
FGC J1739.2 -2530	2.16	3.02	
FGC J1754.9 -2609	3.45	-0.35	
FGC J1802.4 -2352	6.26	-0.67	
FGC J1739.3 -3056	357.57	0.111	1FIG J1740.1-3057
FGC J1742.7 -3005	358.69	-0.066	
FGC J1742.7 -2907	359.5	0.438	
FGC J1739.1 -2931	358.75	0.903	
FGC J1730.5 -3353	354.09	0.078	1FIG J1730.2-3351, G354.1+00.1 [52]
FGC J1752.6 -3029	359.45	-2.101	
FGC J1758.5 -3028	0.089	-3.187	
FGC J1812.9 -3145	0.47	-6.5	NGC 6569 [51]
FGC J1756.4 -2440	4.89	0.11	
FGC J1742.9 -3050	358.08	-0.51	
FGC J1744.6 -2918	359.56	-0.0058	1FIG J1745.0-2905
FGC J1744.5 -2851	359.95	0.245	
FGC J1733.9 -2948	357.9	1.7	
FGC J1801.7 -2324	6.6	-0.3	1FIG J1801.4-2330
FGC J1759.5 -2310	6.54	0.26	
FGC J1757.2 -2411	5.4	0.21	
FGC J1751.7 -2657	2.39	-0.12	
FGC J1747.4 -2809	0.86	0.07	G00.9+00.1 [52], PSR J1747-2809 [50]
FGC J1743.7 -2950	359.02	-0.12	
FGC J1733.3 -3318	354.89	-0.1	Liller 1 [51]
FGC J1729.9 -3423	353.61	-0.105	
FGC J1725.9 -3429	353.05	0.534	
FGC J1800.9 -2353	6.09	-0.394	

Table 1: Point Sources detected with $TS \geq 55$ for the $15^\circ \times 15^\circ$ region about the Galactic Center. The last column displays 1FIG [9] associations as well as spatial overlaps with tentative multi-wavelength counterparts. We use the globular cluster catalog [51], ATNF pulsar catalog [50] and the Green’s SNR catalog [52].

Name	TS	$F_{1-100 \text{ GeV}}$ $\times 10^{-9} [\text{ph cm}^{-2} \text{ s}^{-1}]$	Spectrum	X-bulge contribution
FGC J1756.0 -2508	225.5	13 ± 1	3.1 ± 0.1	0.0
FGC J1801.3 -2449	124.4	10.3 ± 0.9	2.7 ± 0.1	0.0
FGC J1744.2 -2932	391.7	1 ± 1	2.4 ± 0.4	0.1
FGC J1739.6 -3022	363.3	14 ± 1	3.0 ± 0.1	0.1
FGC J1735.9 -3028	163.3	8.0 ± 0.8	2.7 ± 0.1	0.0
FGC J1737.2 -3145	177.7	14 ± 1	2.9 ± 0.1	0.0
FGC J1734.9 -3228	91.3	10 ± 1	2.8 ± 0.1	0.0
FGC J1731.6 -3235	143.3	11.5 ± 0.9	3.0 ± 0.1	0.0
FGC J1729.1 -3443	109.2	8 ± 1	2.9 ± 0.1	0.0
FGC J1736.5 -3420	101.9	5.1 ± 0.6	2.8 ± 0.1	0.0
FGC J1759.7 -2353	100.4	7 ± 3	2.4 ± 0.1	0.0
FGC J1758.1 -2320	59.7	4 ± 1	2.5 ± 0.2	0.0
FGC J1727.7 -2302	71.5	1.7 ± 0.3	2.3 ± 0.1	0.0
FGC J1711.3 -3008	78.2	2.3 ± 0.3	2.8 ± 0.1	0.0
FGC J1733.1 -2910	71.3	2.8 ± 0.6	2.6 ± 0.2	0.6
FGC J1805.1 -3619	64.9	1.6 ± 0.2	$2.0 \pm 0.1, 1.7 \pm 0.3$	0.0
FGC J1734.6 -2202	73.7	2.9 ± 0.3	4.1 ± 0.3	0.2
FGC J1739.2 -2530	56.2	2.6 ± 0.6	2.6 ± 0.2	0.2
FGC J1754.9 -2609	72.9	8.8 ± 0.9	3.0 ± 0.2	0.0
FGC J1802.4 -2352	77	8 ± 2	2.4 ± 0.1	0.0
FGC J1739.3 -3056	111.3	11 ± 1	3.0 ± 0.1	0.0
FGC J1742.7 -3005	161.2	7 ± 2	2.9 ± 0.2	0.0
FGC J1742.7 -2907	90.4	6 ± 1	3.0 ± 0.2	0.4
FGC J1739.1 -2931	84.5	6.6 ± 0.8	3.3 ± 0.2	0.5
FGC J1730.5 -3353	113.2	9 ± 1	3.0 ± 0.2	0.0
FGC J1752.6 -3029	62.8	2.1 ± 0.5	3.1 ± 0.3	0.7
FGC J1758.5 -3028	63.9	1.2 ± 0.3	2.2 ± 0.2	0.5
FGC J1812.9 -3145	61.7	1.3 ± 0.2	2.2 ± 0.1	0.0
FGC J1756.4 -2440	59.7	6 ± 1	2.6 ± 0.2	0.0
FGC J1742.9 -3050	66.3	8 ± 2	2.7 ± 0.2	0.0
FGC J1744.6 -2918	84.5	0.9 ± 0.4	1.7 ± 0.3	0.1
FGC J1744.5 -2851	65.7	4 ± 2	2.8 ± 0.4	0.4
FGC J1733.9 -2948	55.8	1.4 ± 0.4	2.1 ± 0.2	0.5
FGC J1801.7 -2324	131.2	16 ± 4	2.6 ± 0.1	0.0
FGC J1759.5 -2310	55	5 ± 2	2.5 ± 0.2	0.0
FGC J1757.2 -2411	59.7	5 ± 1	2.2 ± 0.3	0.0
FGC J1751.7 -2657	101.1	11 ± 1	3.1 ± 0.2	0.0
FGC J1747.4 -2809	56	10 ± 2	2.7 ± 0.2	0.0
FGC J1743.7 -2950	56.8	8 ± 2	3.1 ± 0.6	0.1
FGC J1733.3 -3318	57.4	6.1 ± 0.9	2.9 ± 0.2	0.0
FGC J1729.9 -3423	57.2	4 ± 1	2.3 ± 0.3	0.0
FGC J1725.9 -3429	55.7	3.1 ± 0.8	2.4 ± 0.2	0.0
FGC J1800.9 -2353	54.6	1.3 ± 0.3	1.2 ± 0.2	0.0

Table 2: Point source spectra and the proportion of the X-bulge contribution to the Poisson amplitude of each new point source. Best-fit fluxes were obtained in the 1 – 100 GeV energy range are denoted by $F_{1-100 \text{ GeV}}$. The spectrum column gives the spectral slope for a power law fit, except in the case where an exponential cutoff model was preferred at $\geq 4\sigma$ level where the E_{cut} in GeV units is also given. Similarly to ref. [18], we combined our energy bands into four larger bands before fitting the spectrum.

E_{\min} (GeV)	E_{\max} (GeV)	E (GeV)	dN/dE (GeV $^{-1}$ cm $^{-2}$ s $^{-1}$)
0.67	0.89	0.77	$(1.8 \pm 0.3) \times 10^{-7}$
0.89	1.2	1.03	$(1.2 \pm 0.1) \times 10^{-7}$
1.2	1.6	1.4	$(6.9 \pm 0.9) \times 10^{-8}$
1.6	2.1	1.8	$(3.8 \pm 0.5) \times 10^{-8}$
2.1	2.8	2.4	$(1.9 \pm 0.2) \times 10^{-8}$
2.8	3.7	3.2	$(9.1 \pm 0.9) \times 10^{-9}$
3.7	5	4.3	$(5.5 \pm 0.7) \times 10^{-9}$
5	6.7	5.8	$(2.2 \pm 0.3) \times 10^{-9}$
6.7	8.9	7.7	$(1.0 \pm 0.2) \times 10^{-9}$
8.9	12	10	$(4 \pm 1) \times 10^{-10}$
12	16	14	$(2.5 \pm 0.7) \times 10^{-10}$
16	21	18	$(1.1 \pm 0.3) \times 10^{-10}$
21	28	24	$(3 \pm 2) \times 10^{-11}$
28	37	32	$(6 \pm 6) \times 10^{-12}$
37	50	43	$(5 \pm 5) \times 10^{-12}$
50	67	58	$(6 \pm 5) \times 10^{-12}$

Table 3: Spectrum of the combined X-bulge and nuclear bulge. The errors in dN/dE include a contribution from the effective area systematic error.

Annulus	0 – 3.5 kpc	3.5 – 8.0 kpc	8.0 – 10.0 kpc
X_{CO}	0.4 ± 0.1	1.1 ± 0.2	3.6 ± 1.3

Table 4: Radial distribution of X_{CO} as obtained from our maximum likelihood estimation using the hydrodynamic gas template models. The quoted values are for the first three annuli and are in units of $10^{20} [\text{cm}^{-2} (\text{K km s}^{-1})^{-1}]$.

Name	l [deg]	b [deg]	Spectral Slope	Spectra Type	X-bulge contribution
J1749.2-2911	0.1921	-0.8134	2.6 ± 0.1	LogParabola	0.7 ± 0.1
J1740.5-2843	359.597	1.0692	2.4 ± 0.1	LogParabola	0.8 ± 0.1
J1754.0-2930	0.4502	-1.8618	2.6 ± 0.1	LogParabola	0.7 ± 0.1
J1740.5-2726	0.6761	1.7336	2.3 ± 0.1	LogParabola	0.7 ± 0.1
J1736.5-2839	359.185	1.8396	2.4 ± 0.2	LogParabola	0.7 ± 0.1
J1734.7-2930	358.26	1.7011	2.5 ± 0.2	LogParabola	0.7 ± 0.1
J1740.5-2642	1.3039	2.1232	2.3 ± 0.2	LogParabola	0.5 ± 0.1
J1736.0-2701	0.5103	2.8019	2.6 ± 0.2	LogParabola	0.6 ± 0.1
J1747.7-2904	0.1257	-0.4741	2.5 ± 0.1	PowerLaw	0.5 ± 0.1
J1800.0-2955	0.7479	-3.2169	2.7 ± 0.1	PowerLaw	0.6 ± 0.1

Table 5: 3FGL point sources which had an X-bulge contribution ≥ 0.5 . See ref. [18] for spectra type definitions.